Underwater Wireless Optical Communication System Channel Modelling With Oceanic Bubbles and Water Constituents Under Different Wind Conditions

Bhogeswara Rao Angara, Palanisamy Shanmugam, and Harishankar Ramachandran

***Abstract*—Optical wireless data transmission from an autonomous underwater vehicle (AUV) to a sea-surface buoy has become a viable solution to support the increasing needs for many applications in the field of marine technology. Despite having unique characteristics and advantages, underwater wireless optical communication remains a challenging field due to the difficulties associated with the harsh marine environments and severe attenuation caused by the bubbles and particulates. This study aims to evaluate the uplink UWOC system in the presence of particles and bubbles under various wind speeds. To calculate the link distances and signal loss between a transmitter and a receiver of the UWOC system, simulations were performed with the inputs of the water optical properties obtained from the Bay of Bengal and Southern Ocean waters and bubble properties derived from the Hall-Novarini (HN) model. Consequently, the normalized received power were calculated for the different receiver configurations and oceanic conditions without and with bubbles. Our results showed that the received power decreased with the increasing wind speeds and smaller bubble populations. The angular and spatial distributions of the received beam increased for smaller bubble populations under high wind speeds. When compared to the clean bubbles, the received power slightly decreased for the non-absorbing coated bubbles with different film thicknesses (0.01 $\sim$ 1.0 μm) and increased for the absorbing coated bubbles with higher thicknesses ($\geq$1 μm). These results will significantly help the system designer to develop and optimize an UWOC system under different bubble populations and wind speed conditions.**

***Index Terms*—UWOC, uplink channel, optical communication, optical properties, bubbles, Monte Carlo method.**

I. Introduction

UNDERWATER Wireless Optical Communication (UWOC) is an emerging technology and has become an important tool for solving a wide range of ocean observation applications such as ocean resources exploration, scientific data collection, maritime archeology, offshore hydrocarbon exploration and production, sea floor survey and climate change impacts on the ocean ecosystem. The UWOC has advantages over the traditional acoustic communication in terms of the power efficiency for high data transfer rate, capability to link autonomous marine platforms, and uniqueness due to high flexibility, low cost and time consumption, low latency and high security. Owing to its high bandwidth and security, UWOC domain has attracted considerable interest from the scientific, commercial and defense sectors because of its potential to replace or complement the traditional communication methods. Taking advantage of the low absorption window of sea water in the blue-green wavelengths of the electromagnetic spectrum, UWOC will provide an efficient communication among the AUVs, ships, underwater sensors, gliders, buoys and submarines for short range applications. The optical communication is less impaired by the multipath and fluid motion effects, shallow bathymetry and boundary interfaces [1], [2]. The UWOC provides robust communication between a transmitter and a receiver within the subsea environment or between the air-water/water-air environment. The limitation of optical communication is associated with high attenuation (absorption and scattering) of the electromagnetic energy by the water constituents (such as phytoplankton, suspended sediments and dissolved organic matter) and wind-wave-generated bubbles. Numerous dedicated research work have demonstrated the design and application of UWOC over short distances in the laboratory setup [3], [4], [5], [6] or field conditions [7], [8]. Such experimental studies have established the optical links in clear water conditions without the bubble effects due to the known limitations. Advancing the UWOC studies requires the different strategies to include the effects of water constituents in coastal regions and bubbles in the near-surface layer. This can be studied with an efficient model to calculate the link distances and signal loss between a transmitter and a receiver.

The light propagation in different oceanic waters is mainly affected by the water constituents (such as algae, suspended sediments and detritus) and bubbles [9], [10], [11]. The oceanic bubbles are abundantly produced by breaking waves in surface waters [12], [13] and formed by ship wakes and other turbulent conditions [14]. Large bubbles (approximately 10 μm) usually occur in near-surface waters and their size and concentration

Manuscript received 8 March 2023; accepted 13 March 2023. Date of publication 17 March 2023; date of current version 29 March 2023. This work was supported by the Ministry of Human Resource Development through the Interdisciplinary Research Program of the Indian Institute of Technology Madras. *(Corresponding author: Palanisamy Shanmugam.)*

Bhogeswara Rao Angara is with the Department of Ocean Engineering, Indian Institute of Technology Madras, Chennai 600036, India, and also with the Department of Electrical Engineering, Indian Institute of Technology Madras, Chennai 600036, India (e-mail: oe17d302@smail.iitm.ac.in).

Palanisamy Shanmugam is with the Department of Ocean Engineering, Indian Institute of Technology Madras, Chennai 600036, India (e-mail: pshanmugam@iitm.ac.in).

Harishankar Ramachandran is with the Department of Electrical Engineering, Indian Institute of Technology Madras, Chennai 600036, India (e-mail: hsr@iitm.ac.in).

Digital Object Identifier 10.1109/JPHOT.2023.3258500

fall off rapidly as the depth increases [9]. Previous experimental investigations in the Southern Ocean under high wind speeds demonstrated that a wind speed of 13 m s^{-1} could generate a wide range of bubbles with a large contribution of the smallest bubbles in the total bubble populations, and penetration depth of the smaller bubbles increases with an increase in wind speed [10]. When a beam of light propagates through an underwater channel in the presence of bubbles, the intensity of light is affected by the refraction and reflection of bubbles at the water-air interface and scattering and absorption of bubble surface [15], [16]. Under the higher wind speeds, the bubble scattering is better pronounced and even higher than that of the particulate scattering in the ocean. Thus, it is crucial to understand the effects of clean and coated bubbles (with different size distributions and coating thickness) on the performance of the uplink UWOC system. According to the previous studies, the bubbles created by wind-induced breaking waves could quickly acquire thin organic films (called coated bubbles) which are composed of lipids and proteins [17]. The mean relative refractive index is $m = n_r + i.\ n_i$ (relative to water), where the real part of the refractive index (n_r) for protein and lipid films is 1.20 and 1.10 respectively and the imaginary part of the refractive index (n_i) varies in the range from 0.001 to 0.006 [18]. The relative refractive index of bubbles with the organic coated film is different from that of clean bubbles ($n_r = 0.75$) and exhibit distinct optical properties (scattering and absorption) [18], [19].

Several researchers have studied the effect of oceanic bubbles (scattering and backscattering) on marine remote sensing applications in the visible and near-infrared wavebands. The bubbles/whitecaps greatly affect the water optical properties and have a pronounced effect on the magnitude and shape in light scattering from the sea surface [20], [21]. The bubbles also make a significant contribution to the backscattering coefficients and upwelling light fields [19], thus increasing the magnitude of remote sensing reflectance and a change in the bidirectional reflectance distribution function (BRDF) and spectral reflectance under high wind speeds [9]. Earlier studies have investigated the vertical (downlink) UWOC channels under different turbulence conditions based on the temperature and salinity profile data [22], [23] and chlorophyll concentration [24]. Other researchers have studied the beam fluctuation and Bit Error Rate (BER) performance of UWOC system in the laboratory conditions with the presence of larger bubbles (in the order of mm) [3], [25], [26]. Recently, a statistical model was developed to estimate the received power using experiment data under different bubble populations [27]. Numerous studies have investigated the effect of bubbles (clean and coated bubbles with 0.1 μm non-absorbing protein film) on the atmosphere-underwater (downlink) laser communication system (a laser source located in the atmosphere and a receiver located at certain depths below the sea surface). Power (channel) losses due to bubbles under high wind speeds were estimated and analyzed [28]. To date, the effects of oceanic bubbles on the performance of uplink/downlink UWOC systems are less explored owing to the different bubble size distributions, bubble characteristics (clean and coated), different-organic-film-coated bubbles and coating thicknesses. Most of the modelling studies have considered only a small population of bubbles ($r_{\min} = 10\ \mu$m) which are non-absorbing coated bubbles with the layer thickness of 0.1 μm [28], [29].

The primary aim of this study is to overcome the limitations currently associated with the vertical UWOC systems. Specifically, this study focuses on the uplink scenario between an AUV and a buoy, which is predominantly constrained by the absorption and scattering of marine particulates. Moreover, the existing systems have not adequately considered the scattering properties of oceanic bubbles generated by wind-induced breaking waves. Despite the increasing demand for UWOC systems to support the various scientific activities and technological applications, the uplink configuration of UWOC systems has not been adequately studied in the literature due to the fluctuating water physical/optical properties in the upper oceanic layer. Limited studies have been conducted to investigate the impact of oceanic bubbles on the performance of uplink UWOC systems, but the critical issues remain unresolved. Such issues are, for example, how the different size bubble populations (clean and coated), different organic thin-film (absorbing and non-absorbing films of lipids and protein composition) coated bubbles, and how the coating thickness of lipids and protein on the bubble surface affect the optical signal under various wind conditions. These issues underscores the need for further investigation into the impact of oceanic bubbles on the performance of uplink UWOC systems.

The present study investigates the influence of upper oceanic bubbles (coated and clean bubbles under different wind conditions) on the dynamic performance of the vertical underwater wireless optical links. Multiple scattering effects due to air bubbles in coastal and open ocean waters can severely degrade the bit error rate (BER) performance of UWOC systems at high data rates for various modulation schemes. Thus, improving our understanding of the impact of air bubbles on the UWOC channel between the AUV and buoy will aid in the design of a vertical UWOC channel that can perform optimally under real oceanic conditions.

The UWOC channel can be studied through either a turbulence model or an attenuation model (scattering and absorption). In the previous studies [30], [31], it was demonstrated that the impact of turbulence on the received signal is low in a highly scattering channel. Most of the turbulence models rely on the refractive index change under due to the fluctuations in ocean temperature and salinity instead of accounting for the various turbulence source effects. Modelling the uplink UWOC system through the oceanic turbulence due to bubbles is currently difficult due to the difficulty in estimating the optical turbulence coefficients (which depend on the rate of dissipation of turbulent kinetic energy) which are largely caused by wind-generated breaking-waves-and other turbulence source effects. The refractive index, salinity and temperature profiles measured at various locations in the Bay of Bengal during April 2017 are shown in Fig. 1. The refractive index is calculated from the temperature and salinity profiles [32]. The depth profiles indicate that fluctuation of the refractive index along the depth is negligible. Moreover, the visible light is strongly affected by the particles and dissolved substances in oceanic water. The present work is focused on the scattering mechanism rather than

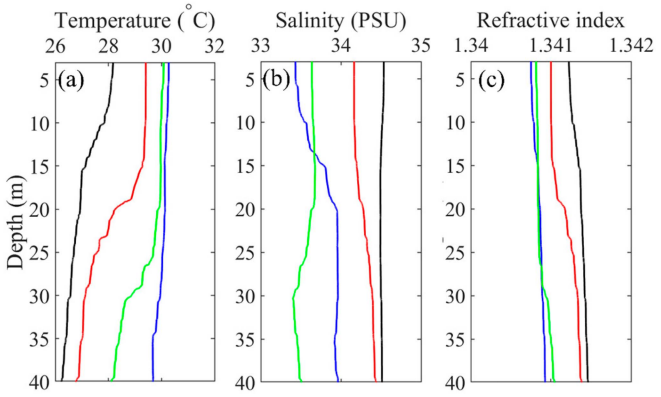

Fig. 1. The depth profiles of (a) temperature, (b) salinity and (c) refractive indices. These data were measured from open sea waters in the bay of Bengal during April 2017.

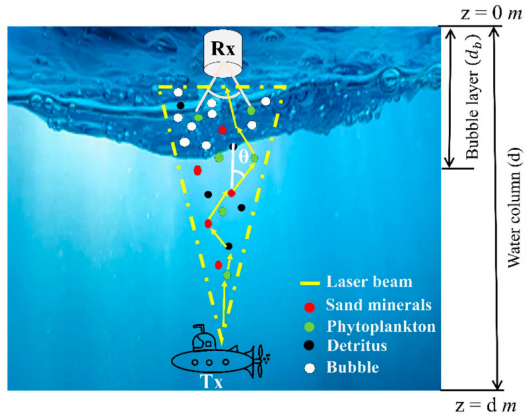

Fig. 2. Schematic of the uplink channel model for an underwater-to-surface (buoy) wireless optical system.

the effect of turbulence and uses the Monte Carlo technique to study the impacts of bubbles on the UWOC system. This study can help in the design and optimization of UWOC systems to mitigate the negative impacts of air bubbles and enable longer link ranges. Further, simulation results will provide useful insights into the estimation of optical turbulence coefficients due to the wind-induced turbulence effects and determination of the necessary power levels for the transceiver to achieve high data rates and low BER for different modulation schemes.

The simulations considered clean and coated bubbles (with variable coating thickness of non-absorbing and absorbing protein and lipid films) to evaluate their effects on the uplink UWOC system and estimate power losses in the underwater channel of 40 m with variable bubble populations and wind speeds. For uplink channel modelling, the light source is located on an AUV (or a floating marine structure) at certain depths from the sea surface and a receiver is placed on a floating buoy near the sea surface. For this analysis, the in-situ measurements of the inherent optical properties of seawater (IOPs such as scattering, attenuation, and scattering phase function) were collected from Bay of Bengal and Southern Ocean waters [10], [33]. The Hall-Novarini (HN) model was used to estimate the bubble number density, which depends on the water depth and wind speed [34].

II. Uplink UWOC Channel Model

This section describes the theoretical background of the model and primary IOP data (absorption, scattering, and attenuation coefficients) for Monte Carlo simulations. For these simulations, the water column is broadly divided into two layers: water column and bubble layer. The schematic diagram of our uplink UWOC channel model along with beam propagation and its interaction with the particles is shown in Fig. 2. Since each photon interacts with a particle, the resultant photons are scattered to angle θ (change of direction of the incident photon) and spread out according to the wavelength and scattering geometry. Here, the laser source is located at a depth of 'd' meters below the sea surface, the receiver is placed at the sea surface ($z = 0$ m), and the bubble layer depth is denoted as 'd_b'.

A. Bubble Generation in the Ocean

Bubbles in the ocean are abundantly produced by wind-induced breaking waves and formed by ship wakes. The bubble number density in oceanic waters generally varies from 10 to 150 μm, bubble sizes are often greater than 10 μm, and bubble sizes and concentrations fall off rapidly with increasing depths. At higher wind speeds, bubbles penetrate deep into the water column where smaller bubbles make a significant contribution to the total bubble population [10]. The previous studies have used in-situ holography observation data to determine the minimum and maximum bubble sizes as 10 μm and 1000 μm [34], [35], [36] and developed an empirical model to estimate the bubble size distributions in seawater, which depend mainly on the wind speed and wave conditions [36].

The present work builds upon the previous studies with a focus on the smaller/persistent bubbles larger than 1 μm and used the Hall-Novarini (HN) model to calculate the bubble size distributions as a function of the wind speed and water depth [34]. Although the HN model was derived for a bubble population with a minimum size of 10 μm, it was extended and validated for a minimum bubble size of 0.5 μm by using experimental data obtained from the Kaylon Randolph team (KRT) [10]. The KRT experiments used the optical measurement techniques to determine bubble size distributions with a minimum size of 0.5 μm, which is the smallest bubble observed in sea water. These experimental data showed that the bubble number density decreases with increasing water depth and increases with increasing wind speed. Using the experimental bubble data from KRT and HN model (for a wind speed of 13 m s^{-1}), three different bubble populations at different depths ($z = 6$, 7, and 8 m)) are shown in Fig. 3, where the shaded area represents the bubble range recorded by averaging the bubble size distributions using the optical measurement techniques at a sampling rate of 1 Hz. The solid and dashed black lines represent the mean of the shaded area bubble population and HN model results respectively. As can be seen, the measured bubble distributions from KRT closely agree with the HN results at different depths.

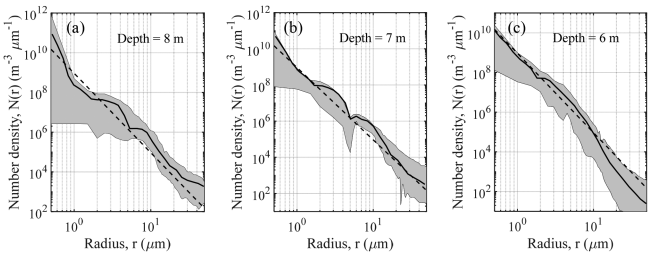

Fig. 3. The optically measured bubble size distributions at high wind speeds ($\approx$ 13 m s^{-1}) and different depths in the Southern Ocean during April 2008 (KRT).

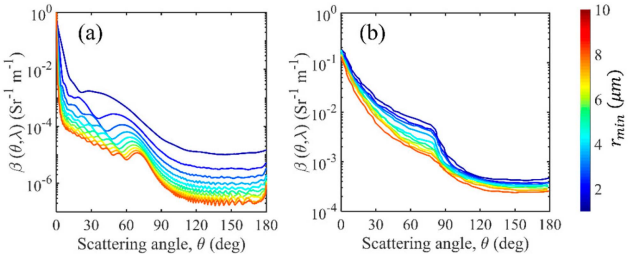

Fig. 4. Effects of the minimum bubble size ($r_{\min}$) on the volume scattering function (VSF) of the different bubble populations in oceanic water. (a) Mie theory simulations for a population of bubbles described by the power law distribution with a fixed maximum bubble size ($r_{\max} = 125$ μm) and a fixed distribution slope ($\alpha = 3.6$)), (b) experimentally measured VSF data for different bubble populations from KRT.

B. Optical Properties of Clean Bubbles

According to the previous study, oceanic bubbles typically follow a power-law distribution with a negative slope (α) [37]. The expression for the power law distributed bubbles is given by

$$p\,(r) = f\,(r_{\min}, r_{\max}, \alpha) \propto r^{-\alpha} \tag{1}$$

where *r* is the bubble size, α is the bubble size distribution slope, $r_{\min}$ and $r_{\max}$ are minimum and maximum bubble sizes in a given population, respectively. When a ray of light strikes the surface of a bubble, there is a well-pronounced scattering pattern in the critical scattering angle region of 50° to 80° which is associated with total internal reflection [18]. This critical-angle scattering pattern was reported in our previous study [38], which focused on the light scattering behaviour of oceanic bubbles based on the theoretical and experimental results and Volume Scattering Function (VSF, $\beta\ (\theta, \lambda)$) data. Fig. 4(a) shows VSF for different bubble populations (with a range of $r_{\min}$ from 1 – 10 μm, $r_{\max} = 125$ μm, and $\alpha = 3.6$) computed from the Mie theory. The Mie theory simulations showed that the angular position of the first dark fringe θ_1 moves in the direction of the critical-angle scattering region as the minimum bubble size increases in accordance with the power-law distributed bubble populations. For better clarity, the measured VSF data for different bubble populations in the Southern Ocean (clear waters with chlorophyll = 0.72 mg m^{-3}, total suspended matter = 0.5 g m^{-3}, wind speed = 13 m s^{-1}, $r_{\min} = 0.5$ μm, $r_{\max} = 125$ μm and $\alpha = 3.6$) are given in KRT. Their experimental results (data reproduced in Fig. 4(b)) were analyzed and compared with the Mie theory, Geometric Optics Approximation (GOA) and empirical methods. Fig. 4(b) shows a distinctive change in the VSF pattern in the critical-angle scattering region for different bubble populations measured at 1 Hz intervals. This critical-angle scattering pattern for distribution of bubbles of sizes greater than 1 μm is well-produced by both Mie theory and experimental results (Fig. 4(a) and (b)). For this analysis, Mie theory simulations were performed for different bubble populations in the absence of water particulates.

The scattering coefficients of different bubble populations ($b_{bub}(z)$, m^{-1})) at depth z were calculated from

$$b_{bub}\,(z) = N\,(z)\,\bar{Q}_{sca}\,\bar{S} \tag{2}$$

where $\bar{Q}_{sca} = 2$ which is the mean scattering efficiency, $\bar{S} \approx 3\pi r_{\min}^2$ which is the geometric mean cross-sectional area of bubbles, and $N(z)$ is the bubble density.

C. Optical Properties of Coated Bubbles

The absorption coefficient *(a)* of oceanic bubbles is negligible in the blue-green wavelength region, but becomes significant in the presence of coated bubbles with the absorbing films with a slightly higher refractive index (lipid, protein film) [19]. The imaginary part of the refractive index of protein-coated films was estimated to be around 0.001 and 0.006. The mean imaginary part of the refractive index is 0.001 for phytoplankton cells, with a maximum value of 0.006 in the visible wavelength of maximum light absorption by the phytoplankton chlorophyll pigment [18]. Earlier studies have reported that the organic film thickness varies from 0 to 1 μm; for example, the organic coating film thickness for oceanic bubbles varies from 0.01–1 μm for proteins (proteoglycans and glycoproteins) and lipids (fatty acids, fatty alcohols, and fatty esters) [18], [19]. Thus, the light scattering patterns and absorption efficiencies of different bubble populations with the refractive index of the lipid and protein films were investigated using the Mie scattering theory. The angular scattering probability of the clean and coated bubbles with non-absorbing and absorbing films are determined by deriving the Cumulative Density Function ($CDF = \hat{\beta}(\theta,\ \lambda)$) of VSF using

$$\hat{\beta}\,(\theta, \lambda) = 2\pi \int_0^{\theta} \tilde{\beta}\,(\theta', \lambda) \sin\theta'\, d\theta', \quad 0 < \hat{\beta}\,(\theta, \lambda) < 1 \tag{3}$$

where $\tilde{\beta}\,(\theta, \lambda) = \beta(\theta,\ \lambda)/b$, which is the scattering phase function (Sr^{-1}), and *b* is the scattering coefficient.

Fig. 5 shows the absorption and scattering efficiencies ($Q_{abs}\ and\ Q_{sca}$) of particles with different refractive indices and organic film thicknesses. Since the coated bubbles with absorbing organic film exhibit the non-zero absorption efficiency, there is a significant absorption of coated bubbles that reduces the total scattering efficiency (Fig. 5). The ratio of the absorption to the scattering efficiency increases with increasing coating film thickness and the scattering efficiency reduces depending on the imaginary part of the refractive index and organic film thickness. The absorption coefficient of the organic film-coated bubbles (with the absorption property) depends on the bubble size as

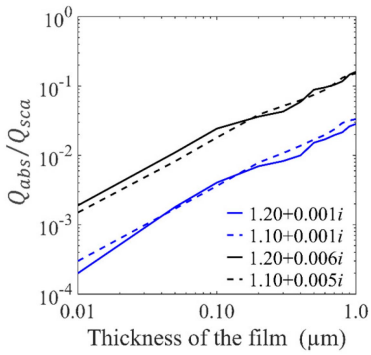

Fig. 5. Variations in the ratio of the mean scattering efficiency to the absorption efficiency of coated bubbles (described by a power-law function) as a function of the coating thickness and refractive index (m) of the organic film.

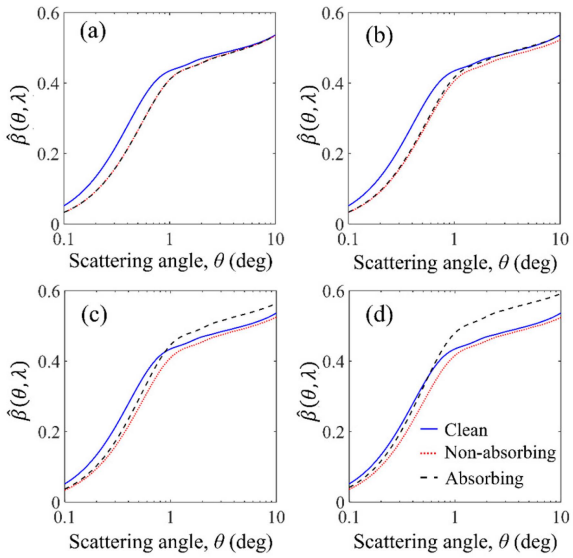

Fig. 6. The CDF ($\hat{\beta}(\theta, \lambda)$) of VSF as a function of the scattering angle determined from the mie theory for different refractive indices (non-absorbing, $m = 1.6 + 0i$ and absorbing, $m = 1.6 + 0.006i$) and organic film thicknesses (t_{film}) on the oceanic bubbles. (a) $t_{film} = 0.01$ μm, (b) $t_{film} = 0.1$ μm, (c) $t_{film} = 0.5$ μm and (d) $t_{film} = 1$ μm. The solid blue line represents the CDF of VSF for clean bubbles.

given by

$$a_{bub}\ (z) = N\,(z)\ \bar{Q}_{abs}\ \bar{S}_{abs} \tag{4}$$

where $\bar{S}_{abs} \approx 3\pi((r_{\min} + t)^2 - r_{\min}^2)$, where t represents the organic film thickness.

Fig. 6 shows the Mie theory simulations of angular scattering probability (CDF of VSF) for different organic thin film thicknesses with a given bubble population (for wind speed = 13 m s^{-1}, $r_{\min} = 10$ μm, $r_{\max} = 125$ μm and $\alpha = 3.6$). As can be seen, coated bubbles with higher absorbing film and larger film thickness have a higher scattering probability over the near-forward angles of 1-10° (Fig. 6(c) and (d)), whereas coated bubbles with the non-absorbing film have reduced scattering probability regardless of the coating film thickness (Fig. 6(a) and (b)) when compared to the clean bubbles. For coated bubbles with higher absorbing film and larger film thickness (the imaginary part of the refractive index = 0.006 for protein and 0.005 for lipids), the amount of absorption efficiency increases from the total extinction efficiency ($Q_{ext} = Q_{abs} + Q_{sca}$) and significantly reduces the scattering efficiency from the case with non-absorbing coated and clean bubbles.

D. Depth Profiles of the In-Situ IOPs Without Bubble Effects

Light propagation through the water column is mainly governed by the absorption and scattering processes, where absorption describes the loss of the light intensity over the propagation distance and scattering describes the direction of scattered photon due to its interaction with a water particle (the sum of these two coefficients gives the attenuation coefficient (m^{-1})). The scattering phase functions ($\tilde{\beta}(\theta, \lambda)$) of particles and molecules are representative of the direction of light scattering within a volume of water. In earlier studies, researchers have reported numerous scattering phase functions models, namely, Henyey-Greenstein (HG) [39], Two-Term-Henyey-Greenstein (TTHG) [40], Fournier-Forand (FF) [41], and Sahu-Shanmugam (SS) [42]. In the present study, we used the depth profiles of IOPs and scattering phase functions collected from the Bay of Bengal (during April 2017) using the LISST-VSF (Sequoia's) and AC-S (WET Labs). These IOPs profiles were obtained from the near-surface layer to 50 m depth. The VSF measurements were recorded when no wave breaks occurred due to winds and showed no critical scattering patterns (due to the bubbles) near the surface. Thus, the IOP profiles are assumed to be free of wind-generated air bubbles. Fig. 7(a) shows the vertical profiles of scattering (b_w) and attenuation (c_w) coefficients which decrease rapidly with depth due to the decreasing particle concentration. The Cumulative Distribution Function (CDF) of the measured VSF (in the absence of bubbles) at discrete depths (solid lines) (see Fig. 7(d)) showed how water particles display more forward scattering at different depths due to the smaller particles [43], [44]. The CDFs for experimentally measured VSF data in Bay of Bengal without the bubbles and Southern Ocean with bubbles displayed a significant amount of light scattering at higher angles.

E. Depth Profiles of the In-Situ IOPs With Bubble Effects

The bubble scattering coefficients (b_{bub}) for different wind speeds and size distributions were calculated from the HN model. The scattering (b_w) and attenuation (c_w) coefficients of water were obtained from the in-situ measurements in clear waters of the Bay of Bengal, and then the total scattering coefficients ($b_t = b_w + b_{bub}$; b_w = scattering coefficient due to the water molecules and particulates) and attenuation coefficients ($c_t = c_w + b_{bub}$; c_w = attenuation coefficient due to the water molecules and particulates) were calculated for different wind speeds (3 to 16 m s^{-1}). According to these data, the bubble layer depth increased with increasing wind speed, which indicates the deeply penetrating bubbles at higher wind speeds [29]. The bubble scattering coefficients (b_{bub}) display higher values in near-surface waters and lower values in subsurface waters (with decreasing depth) due to a decay in the bubble number density. This study considered the bubble populations of different size

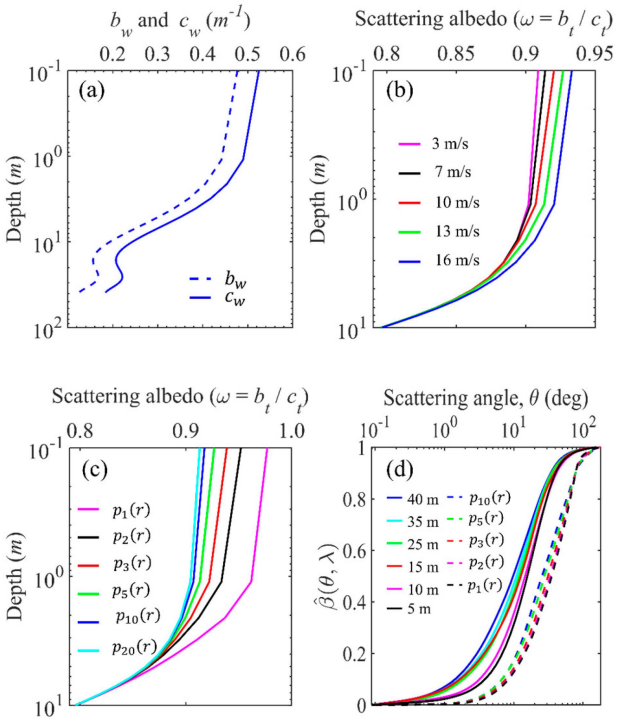

Fig. 7. The depth profiles of (a) attenuation and scattering coefficients (without bubbles), (b) single scattering albedo for different wind speeds, (c) scattering albedo for different bubble size populations, (d) CDF of phase functions at discrete depths (z) (the solid lines represent CDF without bubbles and dashed lines represent the CDF with bubbles). These data came from open sea waters in the bay of Bengal during April 2017, HN model results, and the Southern Ocean during April 2008 (KRT) (CDF).

TABLE I
BUBBLE SIZE DISTRIBUTIONS ($p(r)$) USED IN THIS STUDY

Bubble distribution function ($p(r)$)	r_{min} (μm)	r_{max} (μm)	α
$p_1(r)$	1	125	3.6
$p_2(r)$	2	125	3.6
$p_3(r)$	3	125	3.6
$p_5(r)$	5	125	3.6
$p_{10}(r)$	10	125	3.6
$p_{20}(r)$	20	125	3.6

distributions at a fixed wind speed of 13 m s^{-1} (Table I). According to the HN model, the bubble number density depends on the minimum bubble size in a given population [34], [45]. The HN model results and experimental data (KRT) showed the increasing b_{bub} for a population of smaller bubbles [10], [18], [29].

The vertical profiles of scattering albedo ($\omega = b_w/c_w$ for the water channel and $\omega = b_t/c_t$ for the water channel with bubbles) were calculated as the ratio of the scattering coefficients to the attenuation coefficients. The scattering albedo determines the scattering probability of photons in the water channel. The scattering albedo profiles showed the higher scattering probability of a photon in the bubble layer as the wind speed increased (Fig. 7(b)). The albedo calculations indicate that a population of smaller bubbles has a higher probability of photon scattering than a population of larger bubbles (Fig. 7(d)).

III. RESULTS AND DISCUSSION

This section presents the UWOC uplink channel simulation results with and without bubbles for different receiver configurations. These simulations were performed using the MC method with the inputs of in-situ optical measurements, KRT measurement data and HN model results. According to the MC method, the incoming photons in the water column are scattered or absorbed depending on the single scattering albedo ($\omega = b_w/c_w$ *or* b_t/c_t). Once a photon moves in a random direction and distance in the water column, whether it is absorbed or scattered is determined by generating a random number ξ from the uniform distribution [01] and comparing that with the albedo. The photon is scattered when $\xi \leq \omega$; otherwise the photon is absorbed by the water particles. When a photon is scattered by a water particle or bubble, the scattering angle of the photon is determined by choosing the corresponding depth profile values of CDF. A detailed discussion on the MC local rules of photon propagation in water can be found elsewhere [9], [28].

In this study, MC simulations were established with a laser source located at a depth of 40 m below the sea surface (00,40), a receiver placed on the sea surface (00,0) m, and different bubble layer depths (d_b) according to the wind speed. Typically, autonomous underwater vehicles (AUV: gliders, submarines and marine robots) move from the sea surface into sub-surface water column (up to 200 m). For a maximum wind speed of 16 m s^{-1}, bubbles can penetrate the water to a depth of 20 m. Thus, to understand the effect of bubbles and particles on the modelling of the UWOC channel, a transmission depth of 40 m was considered in our simulation. The bubble layer depths (as determined by HN model) are 5, 7, 10, 15 and 20 m for the wind speeds of 3, 7, 10, 13 and 16 m s^{-1} respectively. For these simulations, in-situ optical measurement data were collected with a 515 nm laser source and used to simulate the UWOC channel characteristics at the same wavelength. The beam width (w) and divergence angle (θ_{div}) of the laser source used for MC simulations are fixed as 1 mm and 1.5 mrad respectively. The smaller beam widths with smaller divergence angles result in low absorption in clear ocean waters, allowing more light to be received by the optical detector [46]. To accurately estimate the effect of bubbles on the UWOC system, we used the in situ profiles of scattering, attenuation coefficients and VSF (rather than the assumed values) for the seawater.

A. *Influence of Clean Bubbles on the Uplink UWOC System With a Fixed Wind Speed and Varying Bubble Size Distributions*

The MC simulation results were used to estimate the received light intensity distribution, an angle of arrival (AOA) of a photon, normalized received power for different receiver apertures and field of views (FOVs). In addition, power losses were estimated for clean and coated bubbles with different wind speeds and bubble size distributions. In the previous section, the light scattering behavior exhibited by the power-law distributed bubbles

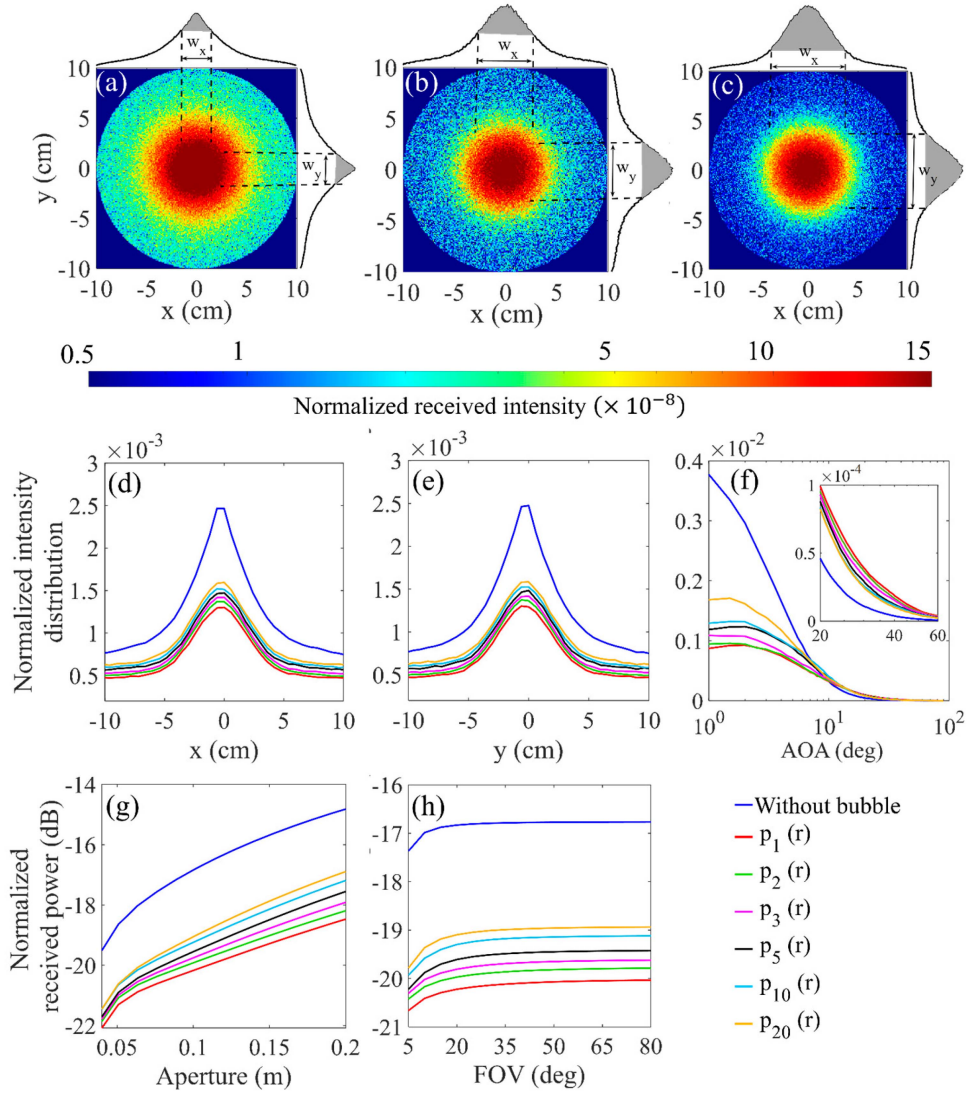

Fig. 8. The variations in the beam profiles after propagating 40 m transmission in seawater with different bubble populations (wind speed = 13 m s^{-1}). The 2D beam profiles of cases (a) without bubbles, (b) with bubble distribution $p_{10}(r)$, and (c) with bubble distribution $p_1(r)$. The 1D beam intensity distribution along (d) x- direction and (e) y- direction. (f) AOA distribution of light intensity. The variation in the received power for a range of (g) receiver apertures (FOV = 180^0) and (h) receiver FOV (aperture = 0.1 m).

was dependent on the $r_{\min}$ parameter with the least amount of change in the $r_{\max}$ and α parameters. Thus, the bubble size distribution parameters were fixed as $r_{\max} = 125$ μm, $\alpha = 3.6$ and $r_{\min}$ from 1 to 20 μm. For this analysis, a fixed wind speed of 13 m s^{-1} was considered for MC simulations. The scattering effect of oceanic bubbles on the UWOC uplink system was analyzed along with the spatial and angular spreading of the received beam. The received light intensity distributions at the receiver plane ($z = 0$ m) after transmission from a depth of 40 m in clear ocean water with and without bubbles (bubble layer depth was up to 15 m) are shown in Fig. 8(a)–(c). Fig. 8(a) shows the received beam profile of the UWOC system without bubbles (considering a calm ocean surface condition with wind speed 0 ms^{-1}). Under such calm ocean surface conditions, the light attenuation is largely influenced by the particles (algae, detritus and sand minerals) only. From Fig. 7(d) it can be seen that the VSF (depth profiles) with water particles have a higher probability at more forward angles than the particles containing bubbles ($p_1(r)$ to $p_{20}(r)$). Thus, due to the presence of bubbles in the water column, the light scatters at higher angles and hence the diameter of the high-intensity beam spot becomes narrower (Fig. 8(b) and (c)) than the UWOC system without the bubbles. Earlier studies [47] (including experimental, theoretical and Mie theory simulations) have indicated that the amount of light scattering by smaller particles is maximal at higher angles. This implies that a laser beam spreads more (with low intensity at its center) for smaller bubbles $(p_1(r))$ than for larger bubbles $(p_{20}(r))$. The light is also strongly attenuated by the smaller bubbles (due to their population density) than by the larger bubbles. In such cases, the UWOC system shows a better performance for larger bubbles than for smaller bubbles. Fig. 8(d) and (e) shows the normalized vertical (y-axis) and horizontal (x-axis) profiles of the received beam intensity distribution for a population of different bubble size distributions. The received

TABLE II
SPATIAL SPREAD OF THE RECEIVED BEAM

Bubble size distribution function ($p(r)$)	w_x (cm)	w_y (cm)
Without bubble	3.0	3.0
$p_1(r)$	7.2	7.3
$p_2(r)$	7.0	7.1
$p_3(r)$	6.7	6.7
$p_5(r)$	6.4	6.4
$p_{10}(r)$	6.1	6.2

TABLE III
SPATIAL SPREAD OF THE RECEIVED BEAM FOR DIFFERENT WINDS

Wind speed (m s^{-1})	w_x (cm)	w_y (cm)
Without bubbles	3.0	3.0
3	3.77	3.76
7	4.86	4.85
10	5.89	5.90
13	7.74	7.73
16	8.63	8.68

Gaussian intensity along the x and y axis (direction) decreases in small bubble populations, because of the multiple scattering of photons depending on the scattering albedo (see Fig. 7(c)). The gray shaded area (top and right panels) of the Gaussian profile in Fig. 8(a)–(c) represents -22 dB power, which is the integral of the light intensity over an interval $[-w_x, w_x]$. Spatial spreading of the received beam (w_x and w_y) was calculated for a received power of -22 dB for each UWOC system (Table II). The beam spread along the x and y axis increases with the decreasing minimum bubble size in the population; hence the UWOC system requires a larger receiver aperture to measure -22 dB power. The spatial spread of the beam in the presence of bubbles is nearly doubled as compared to the spatial spread of the beam in the absence of bubbles.

When the photons interact with water particles or bubbles, multiple scattering contributes to the received photon intensity by the detector at an angle of arrival (AOA). Our simulations showed that the light beam arriving at the receiver plane suffers intensity and spatial spread losses and affects the angular spreading of the received photons (indicating how the light intensity is distributed over the angle of arrival). Based on the analysis of the intensity distributions over the AOA, it was observed that scattering by the underwater bubbles not only affects the spatial spreading but also the angular spreading of the light beam in an UWOC system.

Fig. 8(f) shows the light intensity distribution versus the AOA for a receiver aperture of 0.2 m. The UWOC channel without bubbles transmits more light intensity (normalized) at a smaller AOA ($<10°$) compared to the UWOC channel with bubbles. The light intensity distribution in the UWOC channel with smaller size bubbles ($p_1(r)$) is more dominant at a higher AOA. Since smaller bubbles cause the light beam to be scattered to higher angles, the light intensity distribution increases with the scattering angle. Further, the angular spread was calculated for a receiver aperture of 0.1 m and received power of -20 dB. The received power decreases with increasing $r_{\min}$ values in the bubble population (*i.e.*, 25.2°, 19.8°, 11.4°, 8.1°, 6.7° and 3.7° for the bubble size distributions $p_1(r)$, $p_2(r)$, $p_3(r)$, $p_5(r)$, $p_{10}(r)$ and $p_{20}(r)$, respectively).

For a fixed receiver aperture size, received power and receiver FOV, the different bubble size distributions were determined for further analysis. The simulation results showed that the normalized received power in the UWOC system is higher without bubbles and the lower received power is associated with the increased probability of photon scattering by oceanic bubbles (Fig. 8(g) and (h)). The maximum power loss observed due to the bubbles is around 3.09 dB for the receiver aperture 0.1 m and FOV 10^0 and bubble distribution $p_1(r)$ ($r_{\min} = 1$ μm), and decreases with increasing $r_{\min}$ values in a given bubble population. Fig. 8(g) shows the received power versus different receiver apertures for different bubble populations, where the power loss due to the bubbles increases as the aperture size increases.

B. Influence of Clean Bubbles on the Uplink UWOC System for a Fixed Bubble Population and Different Wind Speeds

This section presents the performance assessment of the UWOC system under different wind speeds. The population of bubbles generated by a power-law was fixed with the parameters $r_{\min} = 5$ μm, $r_{\max} = 125$ μm and $\alpha = 3.6$. As discussed earlier, the bubble number density increases with the wind speed which causes an increase in the scattering coefficient. The 2D beam arriving on the receiving plane (z = 0 m) after transmission over a 40 m channel in clear water (without bubbles) is shown in Fig. 9(a). The profiles of the beam collected by the receiver after passing over a 40 m water channel with a layer of bubbles (different wind speeds) are shown in Fig. 9(b) and (c). For UWOC channel with the bubble plumes, the centre of the beam spot becomes narrower as the photons are scattered more times under higher wind speeds and bubble layer depths. The beam profile in the UWOC channel at a wind speed of 16 m s^{-1} showed a decrease of its intensity as compared to the beam profile at a wind speed of 10 m s^{-1}. With the increase of scattering events, the absorption probability increases (see the scattering albedo in Fig. 7(b)) and causes the beam intensity losses. The received beam intensity profiles (along the x and y directions) in the UWOC channel for different wind speeds are shown in Fig. 9(d) and (e). The spatial spread of the received beam (received power of -22 dB) for each UWOC system are shown in Table III. The received beam intensity distribution over the AOA of photons (for a receiver aperture of 0.2 m) at different wind speeds is shown in Fig. 9(f). The MC simulations (for a -20 dB received power) showed how the angular spread varies and increases with increasing wind speeds (1.4°, 2.6°, 3.7°, 8.1°, and 18.2° at a wind speed of 3, 7, 10, 13 and 16 m s^{-1} respectively).

Fig. 9(g) shows the channel losses without bubbles which increase with increasing bubble populations at higher wind speeds. The channel losses (P_L) were estimated from the MC

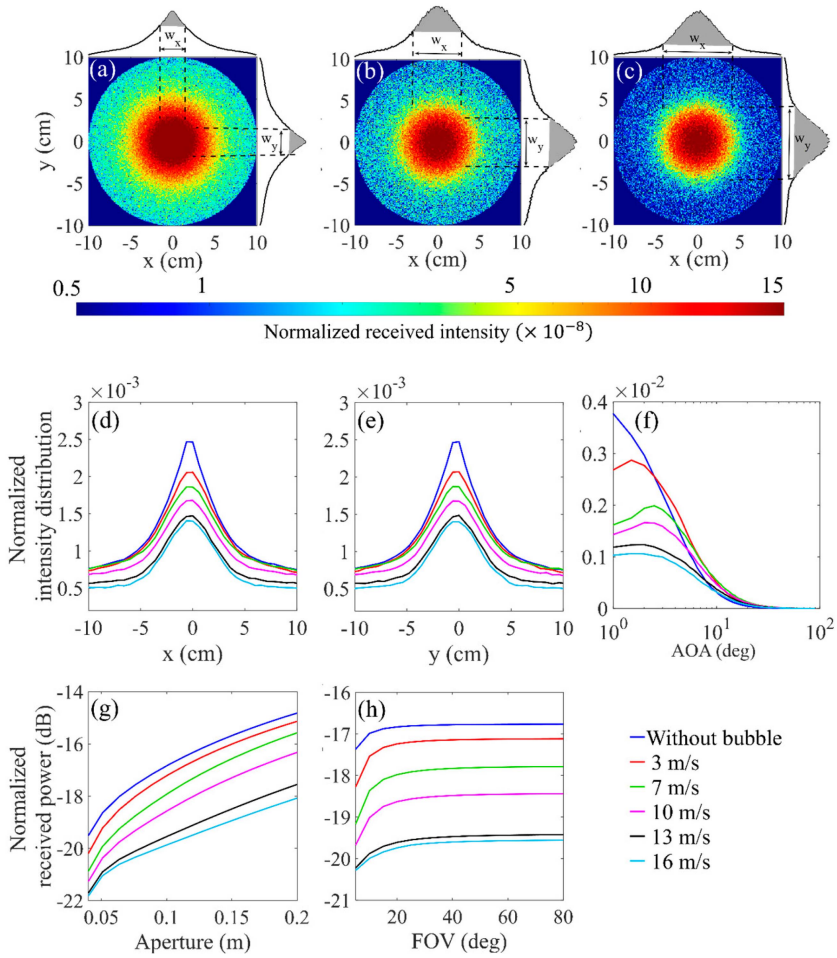

Fig. 9. The variations in the beam profiles after propagating 40 m transmission in seawater with different bubble populations. The 2D beam profile of (a) UWOC channel without bubbles and with bubbles at the wind speeds of (b) 10 m s^{-1} and (c) 16 m s^{-1}. The 1D beam intensity distribution along (d) x- direction (e) y- direction. (f) AOA distribution of light intensity. The variation in the received power for a range of (g) receiver apertures (FOV $= 180^0$) and (h) receiver FOV (aperture $= 0.1$ m).

simulations for the receiver configurations of 0.1 m aperture and 10° FOV ($P_{wob} - P_{wb}$; P_{wob} and P_{wb} are the received power for the cases with bubbles and without bubbles). The estimated channel losses (P_L) were 0.55, 1.38, 2.02, 2.89 and 3.21 dB at the wind speeds of 3, 7, 10, 13 and 16 m s^{-1} respectively. Fig. 9(h) shows the variations of the received power for different FOVs and wind speeds. These results indicate that mild winds have a minimal channel loss with a higher receiver FOV.

C. Impacts of Coated Bubbles on the Uplink UWOC System

This section presents the performance assessment results for the UWOC links in the presence of clean and coated bubbles (non-absorbing and absorbing film of lipids and proteins with different film thicknesses). Here the wind speed was considered as 13 m s^{-1} and the scattering and absorption coefficients of coated bubbles (described by a power law distribution with $r_{\min} = 10$ μm, $r_{\max} = 125$ μm and $\alpha = 3.6$) were calculated using the Mie theory (4) and HN model. Note that the film thickness of a coated bubble in a given bubble population is not uniform and varies from 0.01 to 1 μm. Thus, it is crucial to assess the performance of an UWOC system with coated bubbles with different film thickness (from 0.01 to 1 μm). Fig. 10 shows the received power for clean and coated bubbles with protein ($m = 1.6 + 0i$ and $1.6 + 0.006i$) and lipid ($m = 1.46 + 0i$ and $1.46 + 0.005i$) layers. The MC simulations showed that the normalized received power is slightly reduced for non-absorbing coated bubbles ($m = 1.6 + 0i$ and $1.46 + 0i$ and thickness from 0.01 to 1 μm) as compared to the clean bubbles (Fig. 10(a) and (c)). Fig. 10(b) and (d) show the normalized received power slightly increasing for the absorbing coated bubbles when compared to the clean bubbles, due to the distinct absorption and scattering properties ($m = 1.6 + 0.006i$ and $1.46 + 0.005i$, with coating thickness greater than 0.5 μm). The absorbing coated film with these bubbles has a non-zero absorbing cross-section and reduces the scattering-cross section as compared to the clean bubbles and non-absorbing coated bubbles (with the negligible absorbing cross-section). Due to the reduced scattering cross-section of the coated bubbles (with the absorbing layer of thickness 1.0 μm), the probability of light scattering at higher angles is lower for coated bubbles than for clean bubbles. The absorption coefficient of the coated bubbles is significantly low

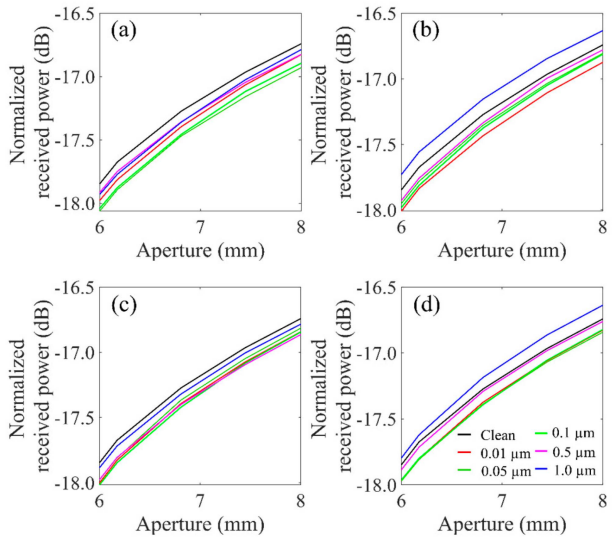

Fig. 10. The variations in the normalized received power with the receiver aperture (FOV = 180^0) for clean bubbles and those coated with the non-absorbing and absorbing organic films of different coating thicknesses. (a) Non-absorbing protein film (m = 1.6 + 0*i*), (b) absorbing protein film (m = 1.6 + 0.006*i*), (c) non-absorbing lipid film (m = 1.46 + 0*i*), and (d) absorbing lipid film (m = 1.46 + 0.005*i*) (for a fixed wind speed of 13 m s^{-1} and a fixed bubble population) in clear waters with a propagation distance of 40 m in the UWOC channel.

at a wind speed of 13 m s^{-1} and increased with increasing film thickness. For a population of bubbles at a wind speed of 13 m s^{-1}, the absorption coefficient (a_{bub}) of the coated bubbles with protein-layered organic film (with the imaginary part of the refractive index of 0.006) is 0.0022, which is maximum at the sea surface and decreases with depth. This indicates that there is a small reduction in the scattering efficiency by coated bubbles, which causes an increase in the received power for coated (absorbing film) bubbles than for clean bubbles.

IV. Conclusion

This study presented the performance assessment results for an underwater optical wireless communication system (UWOC) operating from an underwater vehicle to a sea-surface buoy in the presence of clean bubbles and coated bubbles with different film types and film layer thicknesses. The effect of these bubbles on the UWOC uplink system was rigorously studied using Monte Carlo technique with the inputs of in-situ seawater optical measurements data. For these simulations, the scattering and absorption properties of both clean and coated bubbles were estimated through the Mie scattering theory and HN bubble population model. The results of the HN model for oceanic bubbles smaller than 10 μm were validated using experimental bubble size distribution data from the Southern Ocean in April 2008 (KRT). The VSF data of clean bubbles were also collected from the cruise experiments in the Southern Ocean. The influence of the bubble number density, bubble size and organic film thickness of coated bubbles on the UWOC uplink channel was further investigated in this study. It was observed that both clean and coated bubbles significantly affect the normalized received power, and spatial and angular spreading of the received beam at the detector. The channel losses were calculated for the UWOC system without and with bubbles under different wind speeds and bubble size distributions. Results showed that the normalized received power decreases with increasing wind speed in the case of clean bubbles. The spatial spread of the beam at the detector was more pronounced for a fixed bubble size at higher wind speeds. And the normalized received power and angular spread of the beam were more affected by different bubble size distributions. The simulation results showed that the normalized received power increases with increasing smallest bubble size in the bubble population. Further analysis of the effects of clean and coated bubbles with different thicknesses of organic films (protein and lipid) on the UWOC system, showed significant variations in the received power by the detector. The normalized received power for non-absorbing coated bubbles (thickness from 0.01–1 μm) decreased slightly compared to the clean bubbles. For bubbles with a higher thickness absorbing coated film (>0.5 μm), there is a slight increase in the normalized received power compared to the clean bubbles. The outcome of this study will be helpful for implementing and analyzing the uplink UWOC system from a variety of underwater to the surface platforms with clean bubbles, non-absorbing bubbles and coated bubbles with different film types (composition) and thicknesses under different wind conditions.

References

[1] R. Qadar, W. Bin Qaim, J. Nurmi, and B. Tan, "Effects of multipath attenuation in the optical communication-based internet of underwater things," *Sensors (Switzerland)*, vol. 20, no. 21, pp. 1–16, 2020.
[2] C. Whitt et al., "Future vision for autonomous ocean observations," *Front. Mar. Sci.*, vol. 7, Sep. 2020, Art. no. 697.
[3] H. M. Oubei, R. T. ElAfandy, K.-H. Park, T. K. Ng, M.-S. Alouini, and B. S. Ooi, "Performance evaluation of underwater wireless optical communications links in the presence of different air bubble populations," *IEEE Photon. J.*, vol. 9, no. 2, Apr. 2017, Art. no. 7903009.
[4] T. Lin, N. Huang, C. Gong, J. Luo, and Z. Xu, "Preliminary characterization of coverage for water-to-air visible light communication through wavy water surface," *IEEE Photon. J.*, vol. 13, no. 1, Feb. 2021, Art. no. 7901013.
[5] Z. Chen et al., "Experimental demonstration of over 14 AL underwater wireless optical communication," *IEEE Photon. Technol. Lett.*, vol. 33, no. 4, pp. 173–176, Feb. 2021.
[6] X. Yang et al., "100 m full-duplex underwater wireless optical communication based on blue and green lasers and high sensitivity detectors," *Opt. Commun.*, vol. 498, 2021, Art. no. 127261.
[7] X. Sun et al., "Field demonstrations of wide-beam optical communications through water-air interface," *IEEE Access*, vol. 8, pp. 160480–160489, 2020.
[8] M. Kong et al., "Survey of energy-autonomous solar cell receivers for satellite–air–ground–ocean optical wireless communication," *Prog. Quantum Electron.*, vol. 74, 2020, Art. no. 100300.
[9] J. Zhang, L. Kou, Y. Yang, F. He, and Z. Duan, "Monte-Carlo-based optical wireless underwater channel modeling with oceanic turbulence," *Opt. Commun.*, vol. 475, 2020, Art. no. 126214.
[10] K. Randolph, H. M. Dierssen, M. Twardowski, A. Cifuentes-Lorenzen, and C. J. Zappa, "Optical measurements of small deeply penetrating bubble populations generated by breaking waves in the Southern Ocean," *J. Geophys. Res.: Oceans*, vol. 119, no. 2, pp. 757–776, Feb. 2014.
[11] D. Stramski, E. Boss, D. Bogucki, and K. J. Voss, "The role of seawater constituents in light backscattering in the ocean," *Prog. Oceanogr.*, vol. 61, no. 1, pp. 27–56, 2004.
[12] E. Lamarre and W. K. Melville, "Air entrainment and dissipation in breaking waves," *Nature*, vol. 351, no. 6326. pp. 469–472, 1991.
[13] S. A. Thorpe and P. N. Humphries, "Bubbles and breaking waves," *Nature*, vol. 283, no. 5746, pp. 463–465, Jan. 1980.

[14] W. H. Munk, P. Scully-Power, and F. Zachariasen, "The Bakerian lecture, 1986. Ships from space," *Proc. Roy. Soc. Math. Phys. Eng. Sci.*, vol. 412, no. 1843, pp. 231–254, Aug. 1987.
[15] P. L. Marston, D. S. Langley, and D. L. Kingsbury, "Light scattering by bubbles in liquids: Mie theory, physical-optics approximations, and experiments," *Appl. Sci. Res.*, vol. 38, no. 1, pp. 373–383, 1982.
[16] F. Onofri, "Critical angle refractometry for simultaneous measurement of particles in flow: Size and relative refractive index," *Part. Part. Syst. Characterization*, vol. 16, no. 3, pp. 119–127, 1999.
[17] R. E. Glazman, "Effects of adsorbed films on gas bubble radial oscillations," *J. Acoustical Soc. Amer.*, vol. 74, no. 3, pp. 980–986, 1983.
[18] X. Zhang, M. Lewis, and B. Johnson, "Influence of bubbles on scattering of light in the ocean," *Appl. Opt.*, vol. 37, no. 27, 1998, Art. no. 6525.
[19] X. Zhang, M. Lewis, M. Lee, B. Johnson, and G. Korotaev, "The volume scattering function of natural bubble populations," *Limnol. Oceanogr.*, vol. 47, no. 5, pp. 1273–1282, 2002.
[20] K. D. Moore, K. J. Voss, and H. R. Gordon, "Spectral reflectance of whitecaps: Their contribution to water-leaving radiance," *J. Geophys. Res.: Oceans*, vol. 105, no. C3, pp. 6493–6499, 2000.
[21] D. Stramski and J. Tegowski, "Effects of intermittent entrainment of air bubbles by breaking wind waves on ocean reflectance and underwater light field," *J. Geophys. Res.: Oceans*, vol. 106, no. C12, pp. 31345–31360, 2001.
[22] M. Elamassie and M. Uysal, "Vertical underwater visible light communication links: Channel modeling and performance analysis," *IEEE Trans. Wireless Commun.*, vol. 19, no. 10, pp. 6948–6959, Oct. 2020.
[23] Y. Lou, J. Cheng, D. Nie, and G. Qiao, "Performance of vertical underwater wireless optical communications with cascaded layered modeling," *IEEE Trans. Veh. Technol.*, vol. 71, no. 5, pp. 5651–5655, May 2022.
[24] A. Jain, B. Debnath, and R. Sharma, "Underwater visible light vertical communication for distinctive chlorophyll," in *Proc. 2nd Int. Conf. Adv. Elect., Comput., Commun. Sustain. Technol.*, 2022, pp. 1–5.
[25] D. Chen, J. Wang, S. Li, and Z. Xu, "Effects of air bubbles on underwater optical wireless communication [Invited]," *Chin. Opt. Lett.*, vol. 17, no. 10, 2019, Art. no. 100008.
[26] M. Singh, M. Lal, S. Gurpreet, S. Hardeep, and K. Priyanka, "Modeling and performance evaluation of underwater wireless optical communication system in the presence of different sized air bubbles," *Opt. Quantum Electron.*, vol. 52, 2020, Art. no. 515.
[27] M. Shin, K.-H. Park, and M.-S. Alouini, "Statistical modeling of the impact of underwater bubbles on an optical wireless channel," *IEEE Open J. Commun. Soc.*, vol. 1, pp. 808–818, 2020.
[28] R. Sahoo and P. Shanmugam, "Effect of the complex air–sea interface on a hybrid atmosphere-underwater optical wireless communications system," *Opt. Commun.*, vol. 510, 2022, Art. no. 127941.
[29] L. Ma, F. Wang, C. Wang, C. Wang, and J. Tan, "Monte Carlo simulation of spectral reflectance and BRDF of the bubble layer in the upper ocean," *Opt. Exp.*, vol. 23, no. 19, 2015, Art. no. 24274.
[30] C. T. Geldard, J. Thompson, and W. O. Popoola, "Effects of turbulence induced scattering on underwater optical wireless communications," Aug. 2020. Accessed: Mar. 21, 2023. [Online]. Available: https://arxiv.org/abs/2008.01152
[31] Y. Ata and O. Korotkova, "Absorption, scattering, and optical turbulence in natural waters," *Appl. Opt.*, vol. 61, no. 15, 2022, Art. no. 4404.
[32] X. Quan and E. S. Fry, "Empirical equation for the index of refraction of seawater," *Appl. Opt.*, vol. 34, no. 18, 1995, Art. no. 3477.
[33] M. Twardowski et al., "The optical volume scattering function in a surf zone inverted to derive sediment and bubble particle subpopulations," *J. Geophys. Res.: Oceans*, vol. 117, no. 2, pp. 1–18, 2012.
[34] R. S. Keiffer, J. C. Novarini, and G. V. Norton, "The impact of the background bubble layer on reverberation-derived scattering strengths in the low to moderate frequency range," *J. Acoustical Soc. Amer.*, vol. 97, no. 1, pp. 227–234, 1995.
[35] H. Medwin, "Instrumentation for in situ acoustical measurements of bubble spectra under breaking waves," *J. Acoustical Soc. Amer.*, vol. 86, no. 2, pp. 739–743, 1989.
[36] M. A. Ainslie, "Effect of wind-generated bubbles on fixed range acoustic attenuation in shallow water at 1–4kHz," *J. Acoustical Soc. Amer.*, vol. 118, no. 6, pp. 3513–3523, 2005.
[37] J. Wu, "Bubble populations and spectra in near-surface ocean: Summary and review of field measurements," *J. Geophys. Res.*, vol. 86, no. C1, 1981, Art. no. 457.
[38] B. R. Angara, P. Shanmugam, and H. Ramachandran, "Inversion of volume scattering function for estimation of bubble size distribution in ocean waters," *IEEE Access*, vol. 9, pp. 135069–135078, 2021.
[39] D. Toublanc, "Henyey–Greenstein and Mie phase functions in Monte Carlo radiative transfer computations," *Appl. Opt.*, vol. 35, no. 18, pp. 3270–3274, 1996.
[40] V. I. Haltrin, "One-parameter two-term Henyey-Greenstein phase function for light scattering in seawater," *Appl. Opt.*, vol. 41, no. 6, 2002, Art. no. 1022.
[41] G. R. Fournier and J. L. Forand, "Analytic phase function for ocean water," *Proc. SPIE,* vol. 69, pp. 194–201, 1994.
[42] S. K. Sahu and P. Shanmugam, "Semi-analytical modeling and parameterization of particulates-in-water phase function for forward angles," *Opt. Exp.*, vol. 23, no. 17, pp. 22291–22307, 2015.
[43] M. Jonasz and H. Prandke, "Comparison of measured and computed light scattering the Baltic," *Tellus B: Chem. Phys. Meteorol.*, vol. 38, no. 2, pp. 144–157, 1986.
[44] X. Zhang, E. Boss, and D. J. Gray, "Significance of scattering by oceanic particles at angles around 120 degree," *Opt. Exp.*, vol. 22, no. 25, 2014, Art. no. 31329.
[45] X. Yu, K. Hendrickson, and D. K. P. Yue, "Scale separation and dependence of entrainment bubble-size distribution in free-surface turbulence," *J. Fluid Mechanics*, vol. 885, pp. 1–12, 2019.
[46] W. S. Tsai, H. H. Lu, H. W. Wu, C. W. Su, and Y. C. Huang, "A 30 Gb/s PAM4 underwater wireless laser transmission system with optical beam reducer/expander," *Sci. Rep.*, vol. 9, no. 1, pp. 1–8, 2019.
[47] J. Stetefeld, S. A. McKenna, and T. R. Patel, "Dynamic light scattering: A practical guide and applications in biomedical sciences," *Biophys. Rev.*, vol. 8, no. 4, pp. 409–427, 2016.